American Mineralogist, Volume 96, pages 42–52, 2011

Spectroscopic characterization of transition metal impurities in natural montebrasite/amblygonite

L.N. Dias,[1] M.V.B. Pinheiro,[1] R.L. Moreira,[1] K. Krambrock,[1,*] K.J. Guedes,[2] L.A.D. Menezes Filho,[3] J. Karfunkel,[3] J. Schnellrath,[4] and R. Scholz[5]

[1]Universidade Federal de Minas Gerais (UFMG), Departamento de Física, ICEx, CP 702, 30.123-970 Belo Horizonte, MG, Brazil
[2]Universidade Federal dos Vales de Jequitinhonha e Mucuri (UFVJM), Departamento de Química, 39.100-000 Diamantina, MG, Brazil
[3]Universidade Federal de Minas Gerais (UFMG), Departamento de Geologia, IGC, 31.270-901 Belo Horizonte, MG, Brazil
[4]Centro de Tecnologia Mineral (CETEM), Ilha da Cidade Universitária, 21.941-908 Rio de Janeiro, RJ, Brazil
[5]Universidade Federal de Ouro Preto, Departamento de Geologia, Escola de Minas, 35400-000 Ouro Preto, MG, Brazil

Abstract

Natural single-crystal specimens of the montebrasite/amblygonite series from Brazil, with general formula $LiAlPO_4(F,OH)$, were investigated by electron microprobe, Raman spectroscopy, X-ray diffraction, and infrared absorption. Since little is known about impurities and their local symmetries, electron paramagnetic resonance (EPR) was applied. Six different paramagnetic impurities and radiation defects were detected by EPR. Three of them, all substituting for Al^{3+} ions, namely, iron (Fe^{3+}), vanadium (V^{4+}), and niobium (Nb^{4+}) impurities were characterized in this work. The Fe^{3+} ($3d^5$)-related EPR spectra and angular dependencies show occupation of low-symmetry sites that are revealed in the high asymmetry parameter of the electronic fine structure, $E/D = 0.27$. Vanadium and niobium impurities are identified through their typical strong hyperfine interactions. Both form interesting examples for which the properties of $3d^1$ ion (V^{4+}) and $4d^1$ ion (Nb^{4+}) in the same host matrix can be compared. It is shown that both ions form complex defects of type VO^{2+} (vanadyl) and NbO^{2+} (niobyl), showing superhyperfine interaction with two equivalent hydrogen ions and not to fluorine. The EPR rotation patterns are analyzed in detail for three mutually perpendicular crystal planes. Spin Hamiltonian parameters are calculated and discussed.

Keywords: EPR, montebrasite, amblygonite, Fe, Nb, niobyl, V, vanadyl

Introduction

Montebrasite and amblygonite are lithium aluminum phosphate minerals that, together with spodumene, are natural resources of Li for an increasing battery market. These two minerals together with apatite are also important as phosphorous source for fertilizers in agriculture. Rarely, they are found with good crystalline quality for the gemstone market. Montebrasite and amblygonite are common minerals in lithium-bearing granitic pegmatites. Amblygonite and fluorine-rich montebrasite occur as primary minerals, whereas fluorine-poor montebrasite occurs as secondary mineral after hydrothermal or metasomatic processes, giving important petrogenetic informations. Montebrasite and amblygonite form a complete solid solution with ideal chemical composition $LiAlPO_4(F_x,OH_{1-x})$. Lithium substitution by Na has been reported, but it should not take part of the montebrasite/amblygonite structure (Groat et al. 1990). Indeed, the sodium equivalent for amblygonite is lacroixite with chemical formula $NaAlPO_4F$. Lacroixite has a monoclinic structure with space group $C2/c$, being isostructural to titanite ($CaTiSiO_5$).

The crystal structures for both compounds montebrasite and amblygonite have been determined initially in the late fifties (Simonov and Belov 1958; Baur 1959), and refined later by Groat et al. (1990). Compared to lacroixite, their space group symmetry is reduced to triclinic $C\bar{1}$ because the Li site position is split into two off-center positions, which depend on the fluorine content. The distance between the two off-center Li positions is about 0.2 Å for montebrasite (OH-rich) and about 0.4 Å for amblygonite (F-rich). Although the structures of both minerals are related to the titanite structure, which is known to contain high concentrations of impurities, for natural amblygonite and montebrasite specimens little is known about impurity substitution, incorporation, color, and their local symmetry.

The triclinic montebrasite (amblygonite) structure $C\bar{1}$ is described by a primitive unit cell with parameters: a = 5.178 (5.19), b = 7.123 (7.12), and c = 5.053 (5.04) Å with α = 112.03° (112.03°), β = 97.9° (97.82°) and γ = 67.81° (68.12°) and Z = 2 (Groat et al. 1990). The crystal structure of montebrasite is shown in Figure 1. The structure is characterized by distorted $AlO_4(OH)_2$ octahedra, which are interconnected along the **c**-axis by (F, OH) ions. Laterally, these are connected by nearly perfect PO_4 tetrahedra. The octahedra and tetrahedra form cavities, which are occupied by Li ions in two slightly different off-center positions. Also the two Al octahedra of the unit cell, $Al(1)O_4(F,OH)_2$ and $Al(2)O_4(F,OH)_2$, are structurally slightly different. For the first octahedra the distances to the oxygen ligands are 1.900, 1.899, and 1.918 Å and for the second one 1.906, 1.856, and 1.920 Å (Groat et al. 2003). If we omit the Li off-center positions the

* E-mail: klaus@fisica.ufmg.br

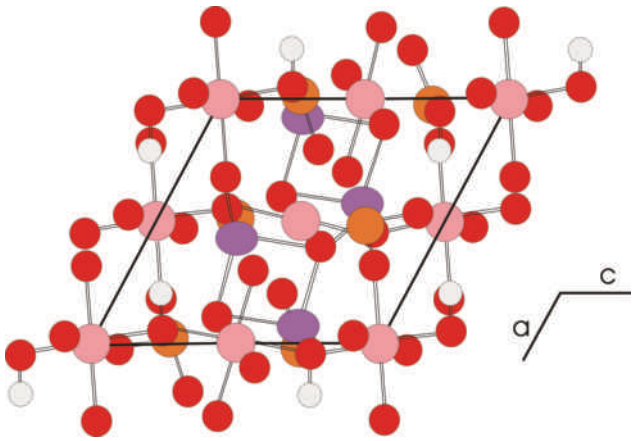

FIGURE 1. Crystal structure of montebrasite projected on the *a*-*c* plane after Groat et al. (1990). The colored balls denote: pink (Al); red (O); orange (P); violet (Li); and white (H). Color online.

space groups of montebrasite (amblygonite) may be described as monoclinic, similar as to titanite, with cell parameters: a = 6.713 (6.645), b = 7.708 (7.733), and c = 7.019 (6.919) Å with β = 117.93° (117.44°) (Groat et al. 1990).

The present work reports, for the first time, electron paramagnetic resonance (EPR) investigations on ferric iron (Fe^{3+}), and on two cationic tetravalent substitutions on Al^{3+} sites, namely V^{4+} (or VO^{2+}) and Nb^{4+} (or NbO^{2+}), in montebrasites. Samples with higher fluorine concentrations do not show such substitutions. Detailed EPR analysis of hyperfine (HF) and superhyperfine (SHF) interactions shows that both the V^{4+} and Nb^{4+} impurity ions are located on Al sites between hydroxyl ions and not fluorine. Those ions have nearly the same electronic configuration, namely $3d^1$ and $4d^1$, respectively. The difference between both configurations is that for 3d transition metal ions the intermediate crystal field explains most properties; whereas for 4d transition metal ions with same number of electrons the strong crystal field approach is more appropriate (Abragam and Bleaney 1986). Therefore, the present work represents an interesting case for which the configurations V^{4+} ($3d^1$) and Nb^{4+} ($4d^1$) in the same host matrix can be compared directly.

SAMPLES

Natural single-crystal specimens of the montebrasite/amblygonite series from Minas Gerais, Brazil, were chosen for our investigation. Three samples denoted AAM (slightly yellow), MSN (slightly green), and MAM (colorless) originate from granitic pegmatites. The first and the latter are situated in the vincinity of Linópolis, Divino das Laranjeiras (Telírio mine and Fazenda Pomaroli mine, respectively) and the second from Sapucaia do Norte (Proberil mine). The Telírio mine is explored periodically since the sixties and has revealed the best montebrasite specimens of the world. Montebrasite occurs in miarolitic cavities in association with brazilianite, beryllonite, apatite-(Ca,F), and eosphorite. In the Proberil mine, lavra Sapucaia, eight new phosphate minerals have been found: frondelite, faheyite, moraesite, barbosalite tavorite, arrojadite-(PbFe), lipscombite, and ruifrancoite (Atencio et al. 2007). The Fazenda Pomaroli mine, a pegmatite 5 m in width, is explored since the nineties. Exceptional high-quality geminated montebrasite were found in miarolitic cavities, some were 20 cm long. Associated minerals are apatite-(Ca,F), eosphorite, frondelite, and zanazziite. Sample AAZ (slightly blue) also originates from a granitic pegmatite, but belongs to the Araçuai district and is located near Coronel Murta (Morro Redondo mine). It corresponds to a primary mineral and is found in association with microcline and quartz.

RESULTS

General characterization of samples

All samples were characterized using different techniques: determination of specific gravities and refractive indices, FTIR spectroscopy, X-ray diffraction (XRD), Raman spectroscopy, and electron microprobe analysis (EMA). Particular attention was given to the fluorine content. The fluorine content measured with EMA is compared to the estimated fluorine concentrations determined indirectly through the other methods. The H_2O and Li_2O contents were calculated by stoichiometry.

Specific gravities were measured by hydrostatic weighing with a Mettler-Toledo CB203 electronic balance. Refractive indices were measured with a Schneider RF2 standard gemological refractometer using monochromatic light (589 nm) and taking readings of two different polished planes in each sample to get the maximum possible birrefringence and n_γ. Infrared absorption measurements (IR) were performed on a Nicolet Nexus 470 transmission spectrometer from 500 to 4000 cm^{-1} at room temperature with spectral resolution of 4 cm^{-1}. Samples were prepared by pressed pellets using a mixture of 300 mg of dry KBr powder and 1.0 mg of fine powdered mineral sample. X-ray diffraction patterns were recorded on a Bruker Explorer spectrometer using Co$K\alpha$ radiation (λ = 1.789 Å). Raman spectra were collected in the spectral range from 100 to 3450 cm^{-1} using a Horiba Jobin Yvon LabRam HR spectroscope with 632.8 nm laser excitation.

Although density measurements are not very useful for the estimation of the fluorine content of amblygonite (Cerná et al. 1973), specimens AAM, MSN, and MAM presented lower values [3.03(1), 3.01(1), and 3.02(1), respectively] when compared to sample AAZ [3.05(1)], indicating a higher F content in the latter. Greiner and Bloss (1987) determined the relationship of the fluorine content to the refractive index γ (n_γ), which decreases at a faster rate than the other indices (n_α and n_β) as a result of the substitution of OH^- by F^- in the montebrasite-amblygonite structure. Fransolet and Tarte (1977) established that, for low sodium content in the amblygonite-montebrasite series, the OH stretching (ν_{OH}) and OH bending (δ_{OH}) vibrations shift linearly and in opposite directions with the fluorine content. Kallio (1978) calculated regression equations based on the angular separation of selected pairs of reflections from X-ray powder diffraction patterns, which decrease or increase as the fluorine content increases. This "four peak" method is especially suitable for the indirect determination of fluorine contents in montebrasite and no internal standard is needed. Rondeau et al. (2006) undertook an investigation of the montebrasite/amblygonite series using Raman spectroscopy and also established regression equations correlating the F content with the position of 3 characteristic Raman peaks and the full-width at medium height (FWMH) of the peak around 3370 cm^{-1}.

For all the above methods, the authors calculated regression equations for the estimation of the fluorine content of montebrasite/amblygonite samples. As our samples all belong to the montebrasite side, we decided to calculate new regression equations based on data presented in the previously mentioned works with fluorine contents below 7.5 wt%. In this specific compositional range, the variations of the physical properties depend linearly

on the fluorine content (Greiner and Bloss 1987; Fransolet and Tarte 1977; Kallio 1978; Rondeau et al. 2006). Results for specimens MAM, MSN, and AAM were all very similar. For clarity, graphical representations of the analyses are shown only for specimens AAM (F-poor) and AAZ (F-rich), illustrating the differences derived from the substitution of $(OH)^-$ by F^-. Figures 2a–2c show, respectively, the infrared absorption spectra, the X-ray diffraction patterns and the Raman spectra.

The fluorine contents of the four samples studied were estimated using regression equations based on data presented in the aforementioned works and are listed in Table 1 together with the measured physical parameters.

Considering the F contents estimated by these independent analyses (Table 1), it is possible to conclude that samples MAM, MSN, and AAM have F concentrations of about 0.5(2) wt% and that sample AAZ has a considerably higher F content, of the order of 5.8(2) wt%.

All samples were also characterized for their chemical compositions and impurity contents with electron microprobe analysis (EMA) using a JEOL 8900R spectrometer. The EMA data obtained in the wavelength dispersive spectrometer mode (WDS) with an operating potential of 15 kV and a beam current of 10 nA are listed in wt% in Table 2. The presented fluorine contents correspond to the mean value from the different indirect measurement (Table 1), i.e., FTIR, X-rays, and Raman. For samples AAM, MAM, and AAZ the phosphorous content was slightly higher and the Al content slightly lower than expected for ideal montebrasite/amblygonite composition (ideal montebrasite: $[P_2O_5]$ 48.48 wt%; $[Al_2O_3]$ 34.82 wt%) (Groat et al. 1990). These values are, however, very similar to that published by Rondeau et al. (2006) with P_2O_5 contents between 49.6–50.5 wt% and Al_2O_3 between 34.4–34.9 wt%. Sample MSN shows a chemical composition similar to that expected for ideal montebrasite. Low vanadium, titanium, and iron impurity contents were found for the first two samples of Table 2, namely AAM and MAM, whereas sample MSN shows only some iron impurity content. For sample AAZ, impurity contents are below the detection limit.

Total formula calculations were performed considering ideal Li_2O content for all samples. The H_2O concentration in wt% can be calculated for the ideal formula of $LiAlPO_4(F_xOH_{1-x})$ using the fluorine concentration as determined by the indirect measurements, which are summarized in Table 2. The results indicate clearly that all samples belong to montebrasite: samples AAM, MSN, and MAM with high OH content, and only sample AAZ with lower OH content.

For the EPR measurements, samples were oriented using the perfect cleavage planes perpendicular to the [100] and [110] axes, respectively, and cut into pieces of about $3 \times 3 \times 2$ mm^3. EPR spectra were recorded on a homemade spectrometer that includes a 500 mW klystron (Varian), a commercial resonance cavity (Bruker), an electro-magnet (Varian) with maximum field amplitudes of 800 mT and a He flux cryosystem (Oxford) for low temperature measurements (5–300 K). For the angular variations, the sample holder fixed to a goniometer was rotated by a stepper motor. Microwave frequency was stabilized by an AFC (automatic frequency control) and measured with a high precision frequency meter (PTS). For *g*-factor calibration the DPPH

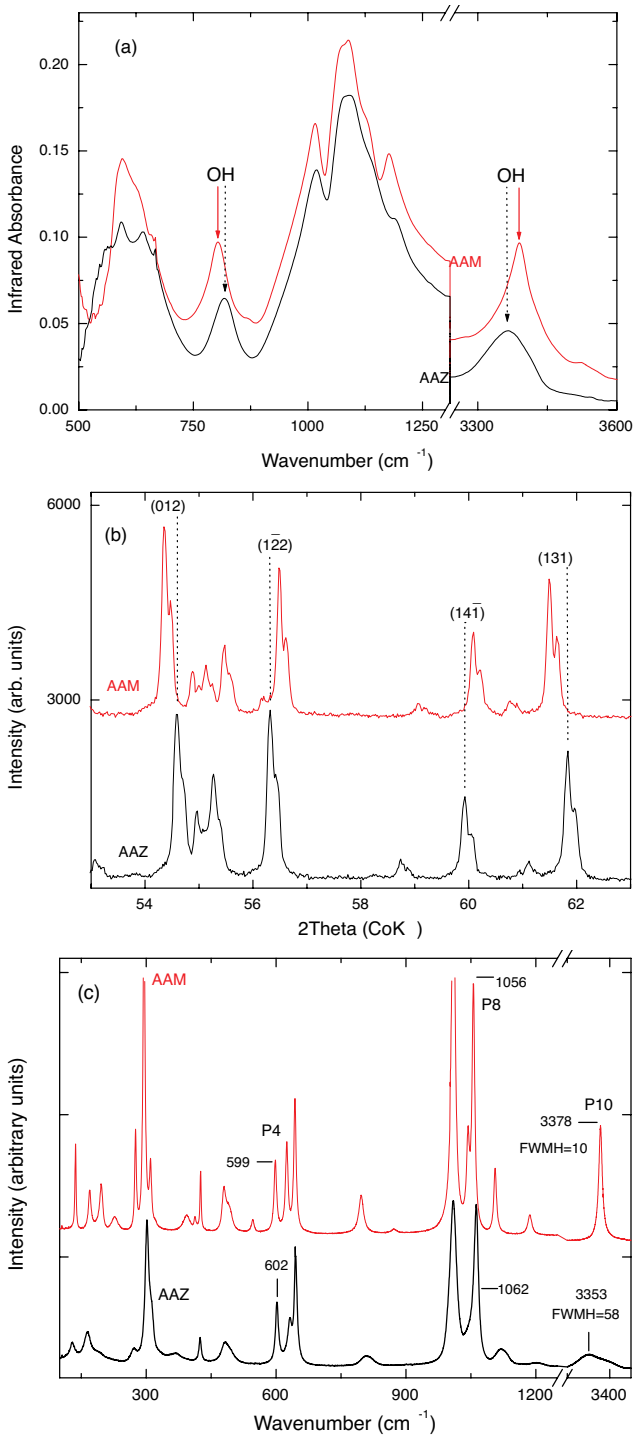

FIGURE 2. (**a**) IR absorption spectra of samples AAM (red) and AAZ (black). OH stretching (ν_{OH}) and bending (δ_{OH}) modes are found at <3400 and >800 cm^{-1}, respectively. (**b**) X-ray diffraction patterns of samples AAM (red) and AAZ (black), showing the shift of a group of four reflections. (**c**) Raman spectra of sample AAM (red) and AAZ (black) indicating the positions of the three characteristic peaks (P_4, P_8, and P_{10}) and the FWMH of P_{10}. Color online.

TABLE 1. Variations of physical parameters and estimated fluorine contents in wt%

Method	Parameters	MAM	MSN	AAM	AAZ
Refractive Index	n_γ	1.647	1.645	1.647	1.618
Index	wt% (F)*	0.13	0.51	0.13	5.60
FTIR	ν_{OH}-δ_{OH} (cm^{-1})||	2584.2	2586.1	2586.1	2547.5
	wt% (F)†	0.96	0.66	0.66	6.80
	2Θ(131–141)#	1.24	1.24	1.22	1.65
	2Θ(1̄22–012)#	1.84	1.85	1.84	1.50
X-ray	2Θ(131-1̄22)#	4.33	4.32	4.33	4.75
	2Θ(141̄–012)#	4.93	4.93	4.95	4.60
	wt% (F)‡	0.56	0.47	0.41	5.06
	P_{10}–P_8||	2322.9	2319.8	2321.8	2290.7
Raman	P_{10} (FWMH)	14	14	10	58
	wt% (F)§	0.44	0.76	0.39	5.65

* $n_\gamma = -0.0053$ wt% + 1.6477; $R^2 = 0.9883$; Equation based on Greiner and Bloss (1987).
† $\nu_{OH} = -6.2811$ wt% + 2590.2; $R^2 = 0.9424$; Equation based on Fransolet and Tarte (1977).
‡ F content estimated using the "four peak method" by Kallio (1978).
§ $\nu_{OH} = -4.9687$ wt% + 2323.9*; $R^2 = 0.9416$ for P_{10}–P_8 and FWMH = 11.324 wt% + 5.8647; $R^2 = 0.9859$ for P_{10}; F content estimated as the mean of the two equations based on Rondeau et al. (2006).
|| Better correlation coefficient using difference between OH absorption bands (ν_{OH}-δ_{OH}) and Raman peaks (P_{10}–P_8) if compared to (Fransolet and Tarte 1977; Rondeau et al. 2006), respectively.
Angular separation of selected pairs of reflections; angles 2θ (Co$K\alpha$) converted to 2θ (Cu$K\alpha$).

TABLE 2. Electron microprobe analysis of montebrasite/amblygonite samples in wt%.

Sample	Na_2O (±0.01)	Li_2O (–)	P_2O_5 (±0.38)	Al_2O_3 (±0.19)	TiO_2 (±0.01)	V_2O_3 (±0.01)	FeO (±0.01)	Nb_2O_5 (±0.01)	H_2O (–)	F (±0.13)	Total (±0.47)
AAM	0.02	10.25	49.58	35.19	0.03	0.00	0.01	0.00	5.89	0.40	101.37
MAM	0.01	10.25	49.99	35.03	0.06	0.03	0.03	0.00	5.83	0.52	101.75
MSN	0.00	10.25	48.57	35.29	0.00	0.00	0.02	0.00	5.80	0.60	100.71
AAZ	0.00	10.25	50.81	33.96	0.00	0.00	0.00	0.00	3.35	5.78	101.72

	Na	Li	P	Al	Ti	V	Fe	Nb	OH	F	
AAM	0.00	1.00	1.04	0.96	0.00	0.00	0.00	0.00	0.95	0.03	3.99
MAM	0.00	1.00	1.03	0.97	0.00	0.00	0.00	0.00	0.94	0.04	3.98
MSN	0.00	1.00	1.00	1.01	0.00	0.00	0.01	0.00	0.94	0.05	4.00
AAZ	0.00	1.00	1.04	0.97	0.00	0.00	0.00	0.00	0.54	0.44	4.00

Notes: Fluorine content was taken as the mean value from Table 1 and from that the water content was calculated. In addition, the chemical compositions are presented in moles.

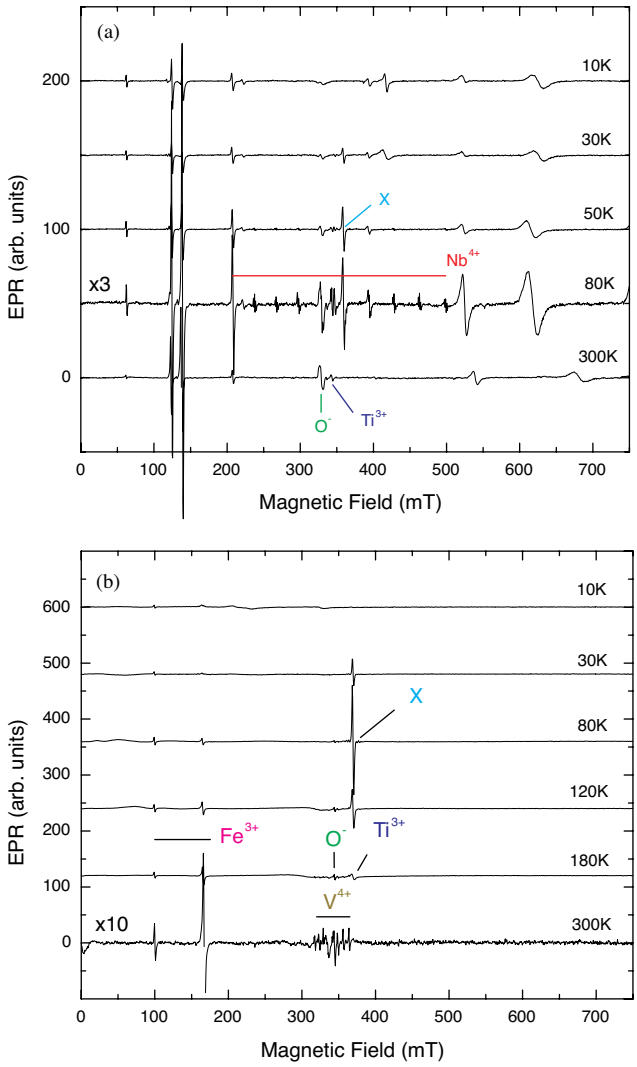

FIGURE 3. Temperature dependence of EPR spectra measured at 9.39 GHz for samples (**a**) MAM for **B**||**b*** and (**b**) AAM single crystals for **B**||**a**, respectively. Arrows mark the different impurities.

standard has been used ($g = 2.0037$). Spectra were recorded as first derivates using the 100 kHz field modulation and Lock-In techniques (EG&G Princeton).

ELECTRON PARAMAGNETIC RESONANCE

Vanadium and niobium-related EPR spectra

Figures 3a and 3b show respectively the temperature behavior of the EPR spectra of montebrasite samples MAM and AAM when the magnetic field **B** is applied along the **b***- and **a**-axes, respectively, with **b*** perpendicular to **a**.

Six different paramagnetic centers due to impurities or radiation-induced centers are identified: V^{4+}, Nb^{4+}, Fe^{3+}, Ti^{3+}, a yet unknown center, called X, and radiation-induced O^- defects. The impurity centers Fe^{3+}, V^{4+}, and Nb^{4+} with $3d^5$, $3d^1$, and $4d^1$ electronic configuration, respectively, are analyzed in this work. The other paramagnetic centers deserve more investigations and will be published in a future work dealing with radiation effects and defects in montebrasite. All transition metal impurities found by EPR in the Brazilian montebrasite samples are in the 10–50 ppm concentration range as determined by a $CuSO_4$ $5H_2O$ standard.

The OH-poor montebrasite AAZ sample does not reveal EPR spectra related to any of the impurities. The V^{4+} spectra were found in the AAM sample (Fig. 3b) at 300 K, whereas the Nb^{4+} was observed in the MAM sample (Fig. 3a) at 80 K. It should be noted that for the microwave powers used (50–100 mW) the vanadium-related EPR spectra saturate completely at about 50 K, while that of niobium at about 30 K. EPR angular dependencies were measured for three mutually perpendicular crystal planes: *ab**a*, *ac**a*, and *c***b***c**. The **b*** and **c*** axes are defined as being perpendicular to the **a**-axis and **b*** close to the crystallographic **b** axis.

For vanadium and niobium ions no electronic fine structure was observed that would be expected for a high-spin system with $S \geq 1$, i.e., for V^{3+} ($S = 1$) or V^{2+} ($S = 3/2$). Therefore, for both vanadium and niobium, $S = ½$ systems have to be assumed. The vanadium isotope ^{51}V has nuclear spin $I = 7/2$ (99.75% abundance) while the ^{93}Nb nuclear spin is $I = 9/2$ (100% abundance).

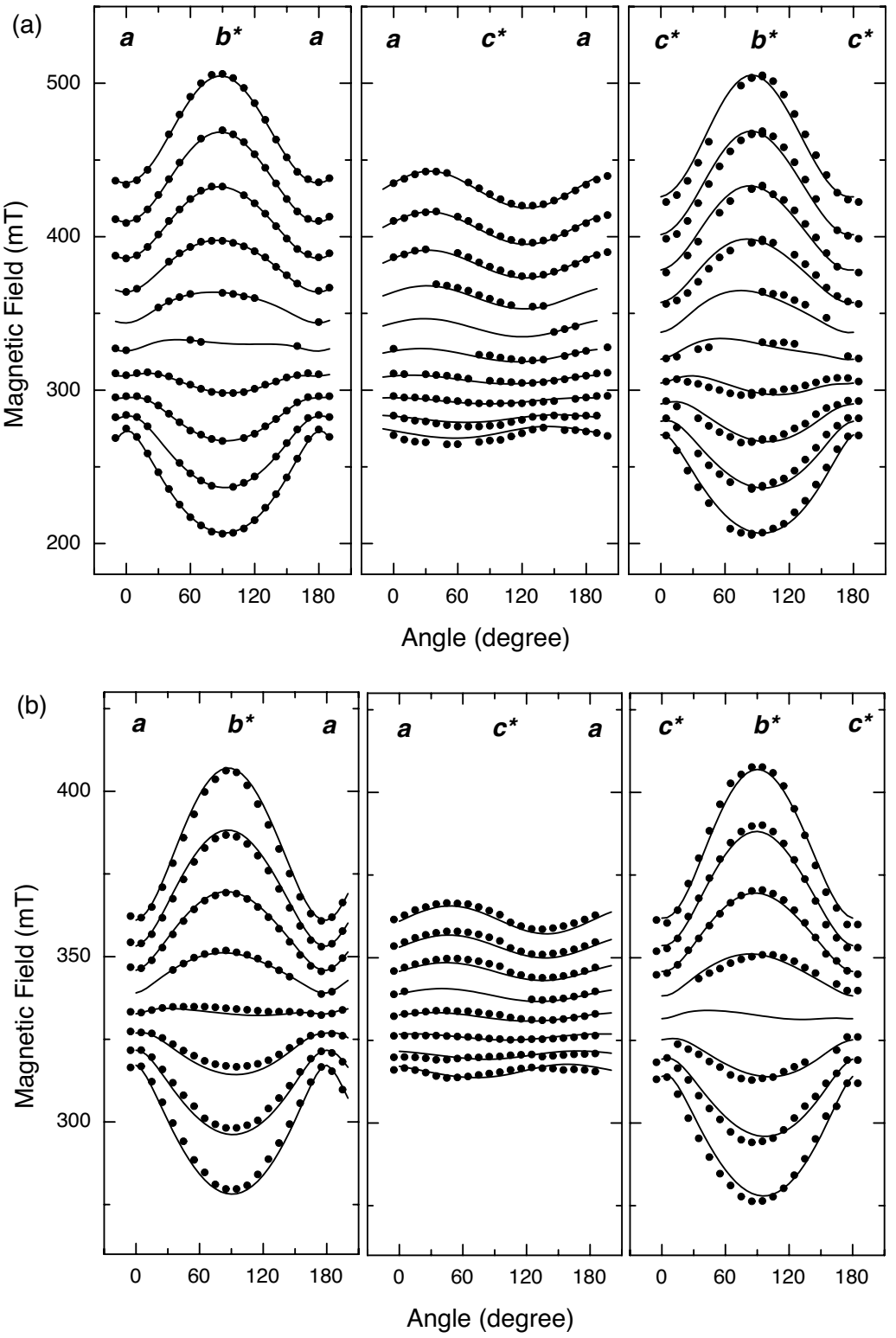

FIGURE 4. Angular dependencies of (**a**) Nb^{4+} EPR spectra measured at 80 K (sample MAM) and (**b**) V^{4+} EPR spectra measured at 300 K (sample AAM) for three mutually perpendicular crystal planes *ab*a*, *ac*a*, and *c*b*c**.

For the first case EPR line packets consisting of 8 lines and for the second case 10 lines are expected due to HF splitting. Figures 4a and 4b show respectively the angular patterns of V^{4+} and Nb^{4+} EPR peak positions for three rotation planes: *ab*a*, *ac*a*, and *c*b*c**. The field positions of EPR lines are shown as dots and calculated angular variations as solid lines. The analysis is described below.

The angular dependencies were analyzed using the following spin Hamiltonian operator

$$H = \beta \mathbf{S}\cdot\mathbf{g}\cdot\mathbf{B} + \mathbf{S}\cdot\mathbf{A}\cdot\mathbf{I} - \beta_n \mathbf{I}\cdot\mathbf{g}_n\cdot\mathbf{B} + \mathbf{I}\cdot\mathbf{Q}\cdot\mathbf{I} + \sum_{i=1}^{2}(\mathbf{S}\cdot\mathbf{T}_i\cdot\mathbf{I}_i - \beta_n \mathbf{I}_i\cdot\mathbf{g}_n\cdot\mathbf{B}) \quad (1)$$

in triclinic symmetry, i.e., without any symmetry relations. The first term belongs to the electronic Zeeman, the second to the

TABLE 3. Spin Hamiltonian parameters from exact diagonalization for $^{93}Nb^{4+}$ ($S = ½$; $I = 9/2$ with 100% abundance) interacting with two equivalent spins $I = ½$

Nb^{4+}	ZZ	YY	XX
g	1.917(1)	1.879(1)	1.846(1)
Θ	31(1)°	98(1)°	60(1)°
Φ	60(1)°	137(1)°	222(1)°
A/h (MHz)	867.7(6)	497.8(9)	420.4(8)
Θ	89(1)°	49(1)°	41(1)°
Φ	90(1)°	181(1)°	360(1)°
A/h (MHz)	104.7(1)	88.8(1)	79.6(1)
Θ	67(1)°	58(1)°	42(1)°
Φ	356(1)°	102(1)°	237(1)°

Notes: *g* = tensor, *A* = *HF* (MHz) of Nb^{4+}, and *T* = *SHF* (MHz) of two equivalent spins with $I = ½$ (100% abundance). Angles Θ and Φ denote polar coordinates of the principal tensor axes. The first is measured from the **c***-axis toward the *a*-*b** plane and the second from the **a** axis inside the *a*-*b** plane.

TABLE 4. Spin Hamiltonian parameters for $^{51}V^{4+}$ (I = 7/2, 99.75% abundance)

V^{4+}	ZZ	YY	XX
g	1.952(1)	1.971(1)	1.984(1)
Θ	110(1)°	115(1)°	33(1)°
Φ	67(1)°	327(1)°	12(1)°
A/h (MHz)	500.6(5)	204(1)	156(1)
Θ	87(1)°	144(1)°	125(1)°
Φ	89(1)°	3(1)°	177(1)°
A/h (MHz)	41.5(1)	37.0(1)	29.2(1)
Θ	73(1)°	75(1)°	23(1)°
Φ	29(1)°	295(2)°	165(1)°

Note: Table 4 uses same notation as in Table 3.

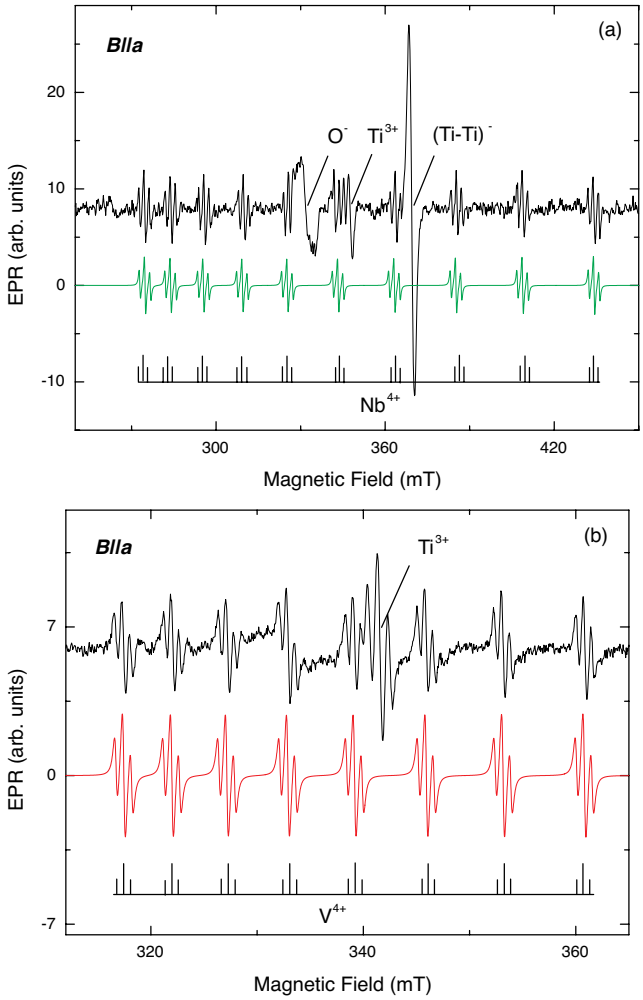

FIGURE 5. SHF-split EPR spectra (black) of (**a**) Nb^{4+} and (**b**) V^{4+} for **B** || **a**-axis. EPR spectrum (**a**) was measured at 80 K in sample MAM, while spectrum (**b**) at 300 K in sample AAM. Calculated spectra for Nb^{4+} (green) and for V^{4+} (red) (for more details see text). Color online.

HF, the third to the nuclear Zeeman interaction, and the fourth to the nuclear quadrupole interaction. The terms under the sum denote the SHF and nuclear Zeeman interaction of the two-ligand interactions. The symbols have their usual meaning (Abragam and Bleaney 1986). The parameters of the spin Hamiltonian were evaluated by fitting simultaneously all line positions in the three mutually perpendicular crystal planes (solid lines in Figs. 4a and 4b) using exact diagonalization of the spin Hamiltonian of Equation 1 for triclinic symmetry. In total, 504 line positions for V^{4+} and 630 for Nb^{4+} were taken into account in the analysis for the three mutually perpendicular crystal planes considering the first three terms of Equation 1. Small misalignments of the exact crystal mounting in the resonance cavity were taken into account. The final fitting parameters of the principal values of the *g* tensor and HF tensor given in MHz are summarized in Tables 3 and 4, together with the polar coordinates of their principal axes and errors.

As one can notice from the angular patterns, only one magnetically independent site is observed for both ions in all three crystal planes and HF interaction is maximal for **B** nearly along **b***. The distance between the HF-split EPR lines increases with increasing magnetic field, better seen in the *ac**a* plane, due to higher order effects in the spin Hamiltonian analysis, i.e., the HF interaction is not small compared with the electron Zeeman interaction.

For both impurity ions, Nb^{4+} and V^{4+}, an additional SHF line splitting is observed. Figure 5 shows typical SHF-split spectra for Nb^{4+} (Fig. 5a, green) and V^{4+} (Fig. 5b, red) when **B** is parallel to **a**-axis for which the SHF splitting is nearly maximal. Measured spectra are shown in black together with calculated spectra using spin Hamiltonian parameters of Tables 3 and 4. For the calculation of the spectra, Lorentzian line shapes with linewidths of ΔB_{pp} = 0.30 mT and *SHF* = 0.72 mT for V^{4+} and ΔB_{pp} = 0.50 mT, *SHF* = 1.72 mT for Nb^{4+} were used. The agreement between calculated and measured spectra is excellent. The splitting is characteristic for two equivalent nuclei with $I = ½$ (100% natural abundance) resulting in three equally spaced EPR lines with intensity ratio of 1:2:1. If we assume that both Nb^{4+} as well as V^{4+} substitutes for Al^{3+} ions then F^- or OH^- are first neighbors of the impurity ion at a distance of 1.904 Å along the **c**-axis. The phosphorous ion ^{31}P has also $I = ½$ with 100% abundance, but is at a much longer distance of 3.11 Å and is therefore not considered as the source of the SHF interaction. Both, the ^{19}F and ^{1}H have nuclear spin $I = ½$ with nearly 100% natural abundance. According to the structure model of montebrasite (see Figs. 1 and 8), the OH^- or F^- anions interconnect the Al^{3+} ions nearly along the **c**-axis and form equivalent neighbors on both sides of the impurity ion.

Figure 6 shows the angular dependencies of the SHF interaction of both transition metal ions in the three crystal planes *ab**a*, *ac**a*, and *c*b*c**. The SHF interaction was determined as the distance between the SHF-split EPR lines. It should be noted

that the SHF interaction is small compared to the HF interaction and therefore does not depend on the considered HF transition. The SHF interaction can be calculated separately in first-order perturbation theory because it is much smaller than the HF interaction.

The angular behavior of the SHF interaction is similar for both ions, V^{4+} and Nb^{4+}, in the *ac*a* plane, with some difference for the other planes *ab*a* and *c*b*c**. Maximum SHF interaction is observed nearly along the **a**-axis for the EPR spectra of both ions, i.e., more exactly at about 20° off **a**-axis in the **ac*a** plane (marked by the arrows in Fig. 6). It should be noted that the SHF

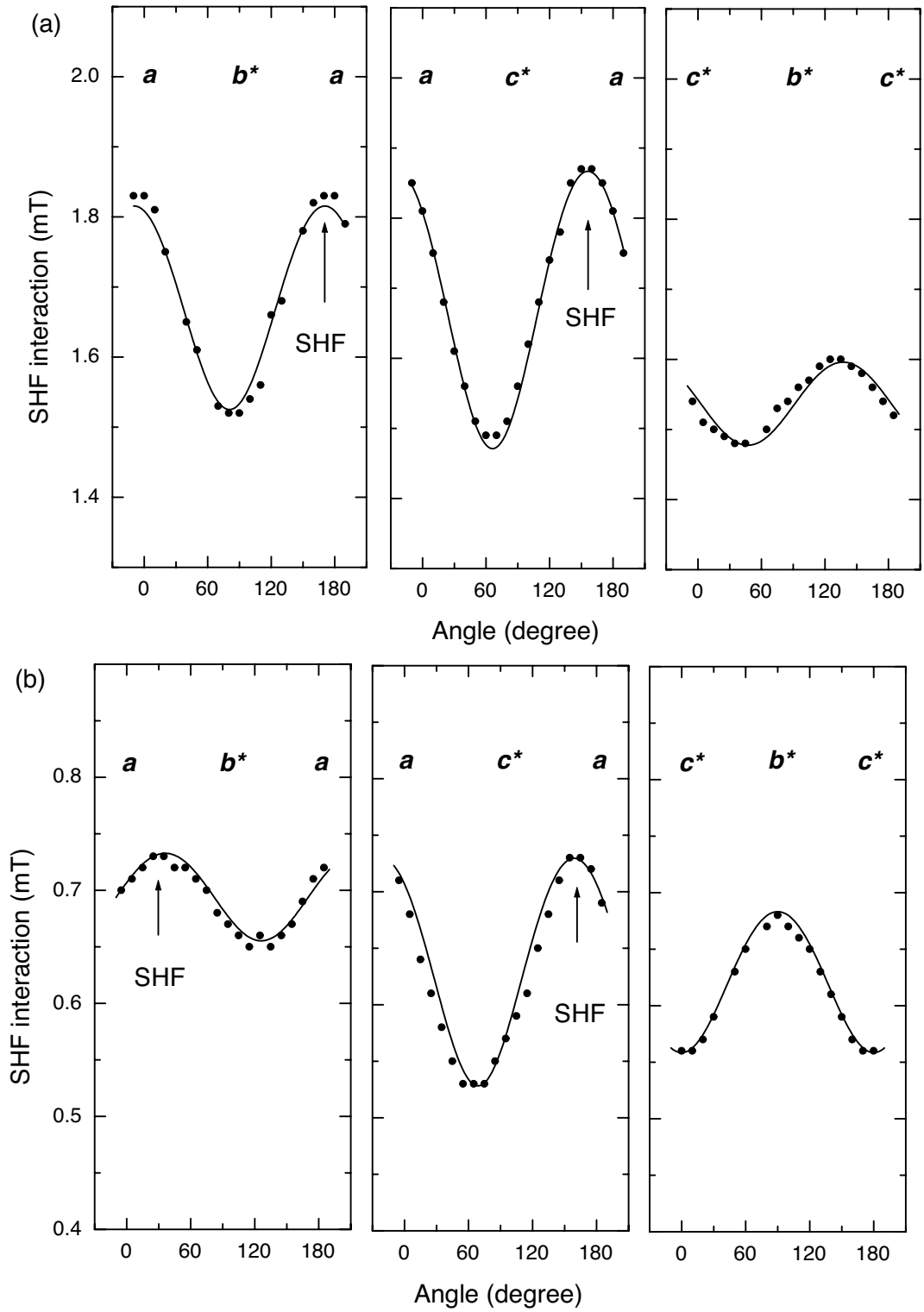

FIGURE 6. Angular dependence of SHF interaction for (**a**) Nb^{4+} in MAM sample and (**b**) V^{4+} in AAM sample in the three crystal planes *ab*a*, *ac*a*, and *c*b*c**. Dots represent experimental line positions and solid lines our fits with obtained values.

interaction for the niobium ion is about 2.5 larger than that for vanadium ion. Within error, the nuclear quadrupole interaction has no influence in the calculation of the EPR spectra as well as on the angular dependencies.

Ferric iron—Related EPR spectra

Figure 7 shows the angular variations of the peak positions of the EPR lines due to Fe^{3+} in the three mutually perpendicular crystal planes *ac*a*, *ab*a*, and *b*c*b** in the montebrasite sample AAM measured at room temperature. The EPR line positions and intensities vary strongly with orientation of the sample with respect to the magnetic field and range from 50 mT to about 800 mT, the limit of our equipment.

The angular dependence of Fe^{3+}-related EPR spectra belong to the high spin state $S = 5/2$ with ground state multiplet $(3d^5)\ ^6S_{5/2}$, typical for intermediate crystal fields (Abragam and Bleaney 1986). The most intense and most isotropic EPR lines are found in low-field region, i.e., about 150 mT (shown by the red dots in Fig. 7). This transition belongs to allowed m_s –1/2 → +1/2 transition of Fe^{3+}.

It should be noted that again only one magnetically inequivalent site is observed for all three measured crystal planes. In contrast to the vanadium and niobium-related EPR spectra SHF interaction is not observed, probably due to larger linewidths. The EPR angular dependencies of Figure 7 were analyzed using the following spin Hamiltonian in triclinic symmetry

$$H = \beta \mathbf{S}\cdot\mathbf{g}\cdot\mathbf{B} + \mathbf{S}\cdot\mathbf{D}\cdot\mathbf{S} + \sum_{m=-4}^{+4} B_4^m O_4^m + g_e\beta B\left[\sum_{m=-2}^{2}\left(B_{2m}^{13}U_{3,2,m}\right) + \sum_{m=-4}^{4}\left(B_{4m}^{13}U_{3,4,m}\right)\right] + g_e\beta B\left[\sum_{m=-4}^{4}\left(B_{2m}^{15}U_{5,4,m}\right) + \sum_{m=-6}^{6}\left(B_{6m}^{15}U_{5,6,m}\right)\right] \quad (2)$$

The first term in Equation 2 corresponds to the electronic Zeeman interaction, the second to the electronic fine structure and the third is due to fourth-order terms S^4 in Stevens notation. The last two terms in brackets in Equation 2 correspond to linear high-spin terms, where $U_{\mathrm{lS,l,m}}$ values, which are tabulated in Table 3 of McGavin et al. 1990, are functions of spherical spin operator tensors, $\mathbf{T}_{\mathrm{l,m}}$. The $B_{\mathrm{lm}}^{\mathrm{lBlS}}$ (i.e., the sets of parameters to be determined in refinement) are components of irreducible tensors of rank *l*. Because of triclinic symmetry, all parameters may contribute to the spin Hamiltonian, i.e., 9, 14, and 22 parameters for S^4, BS^3, and BS^5, respectively (McGavin et al. 1990). The method for the calculation of the angular dependencies was the same as used for the vanadium and niobium. In total, 204 line positions were taken into account in the analysis. The final fitted line positions are plotted in Figure 7 as solid lines and final spin Hamilton parameters collected are listed in Table 5. The fine-structure parameters $|D|$ and $|E|$ are 9.57(1) and 2.55(1) GHz, respectively, resulting in an asymmetry ratio

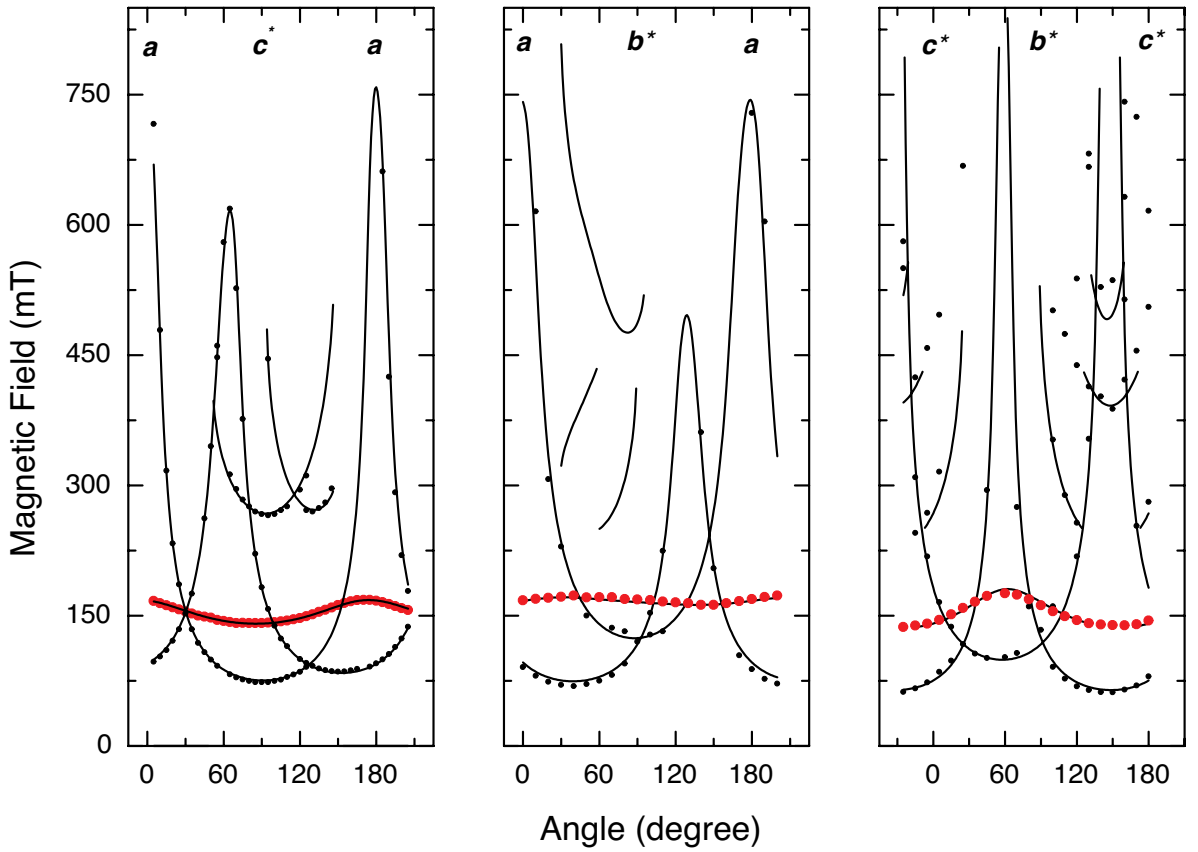

FIGURE 7. Angular dependencies of Fe^{3+}- related EPR spectra in the magnetic field region from 0–800 mT measured at 300 K for sample AAM in three mutually perpendicular crystal planes *ac*a*, *ab*a*, and *b*c*b**. Dots correspond to line positions and solid lines to calculations (see text).

E/*D* of 0.27. The absolute sign of the electronic fine-structure parameters was determined from the temperature dependence of the intensity of the EPR lines. The low field lines decrease in intensity in favor for the high field lines, which means that both fine-structure constants have negative signs similar to ferric iron in euclase (Guedes et al. 2006; Abragam and Bleaney 1986). It should be noted that the terms in S^4 have a strong influence on the angular dependence of the EPR lines of Fe^{3+} in montebrasite. However, the higher order terms BS^3 and BS^5 do not contribute within error. The S^4 terms increase the anisotropy of the *g* tensor, however, the medium *g* value is still 2.015 and consistent with the expected value for Fe^{3+}.

Discussions

The EPR spectra due to vanadium and niobium analyzed in this work belong to spin $S = ½$ systems as indicated by the missing electronic fine structure, which is in accordance with V^{4+} and Nb^{4+}. V^{3+} and V^{2+} have spin $S = 1$ and $S = 3/2$, respectively. The identification as vanadium and niobium-related EPR spectra is based on their typical HF interaction in case of vanadium 8 HF EPR lines (^{51}V: $I = 7/2$ with 99.75% abundance) and for niobium 10 HF EPR lines (^{93}Nb: $I = 9/2$ with 100% abundance). Other isotopes that have nuclear spin $I = 7/2$ (100% abundance) are ^{45}Sc, ^{59}Co, ^{139}La, ^{165}Ho, ^{181}Ta, and $I = 9/2$ (100% abundance) ^{113}In and ^{115}In, and ^{209}Bi can be excluded as candidates for the EPR spectra measured in the montebrasite samples because of ionic radii and valence state mismatch (Abragam and Bleaney 1986).

The V^{4+} ($3d^1$) and Nb^{4+} ($4d^1$) have nearly the same electronic configuration. The difference between both configurations is that for 3d transition metal ions the intermediate ligand field explains most properties; whereas for 4d transition metal ions with the same number of electrons the strong field approach is more appropriate (Abragam and Bleaney 1986). The wave functions for 4d transition metal ions have the same angular dependence as that for 3d ions, but their radial parts differ in that 4d wave functions have one node while 3d none. Near the nucleus the radial 4d wave functions have amplitudes that increase rapidly with the atomic number. Therefore, larger hyperfine values and larger spin-orbit coupling are expected for 4d ions when compared to 3d ions (Abragam and Bleaney 1986).

It is difficult to explain the features of the observed spin Hamiltonian parameters of $3d^1$ and $4d^1$ in octahedral field. We expect a Γ_5 triplet state and Γ_3 doublet state as ground state and excited state, respectively. Admixtures from the Γ_3 doublet are expected to be low because spin-orbit coupling is small. The unusual *g* values of Ti^{3+} ($g_\parallel = 2.00$ and $g_\perp < 0.1$), which is isoelectronic to V^{4+} ($g_\parallel = 1.43$ and $g_\perp < 0.2$) in Al_2O_3 have been explained by a dynamic Jahn-Teller effect (Joyce and Richards 1969; Macfarlane et al. 1968).

The observed vanadium-related EPR spectra in montebrasite are much better explained by a vanadyl ion $(VO)^{2+}$ that has spin $S = ½$ and because of the complex *g* values much closer to the *g* factor of the electron. Its formation may be induced by a dynamic pseudo Jahn-Teller effect. Such approach has been suggested for Ti^{3+} in $LiNbO_3$ and $LiTaO_3$ (Thiemann et al. 1994). Because the niobium-related EPR spectra are comparable with that of vanadium we assume that niobium also forms the complex niobyl $(NbO)^{2+}$ with $S = ½$. The formation of this complex may also be induced by a Jahn-Teller effect.

The formation of the vanadyl molecule VO^{2+} is generally attributed to the coupled substitutions of, for example, $(Al\text{-}OH)^{2+}$. The molecule is characterized by a very short bond distance of about 1.6 Å (Vassilikou-Dova 1993). In general, both the *g*-tensor and the HF tensors are nearly axial with $g_\parallel < g_\perp$, indicating a tetragonally compressed octahedron, and both the parallel components, $g_\parallel$ and $A_\parallel$, along the short V-O bond. In sixfold coordination, the EPR spectra of vanadyl are observable at room temperature, whereas for fourfold coordination lower temperatures are required. Although the symmetry of the *g* and HF tensors are actually orthorhombic or lower, they can be approximated by axial tensors. From our analysis (see Tables 3 and 4) we found that the principal tensor axes of *A* of both ions, $A_\parallel$ or A_{zz}, are nearly along the **b***-axis. From that we conclude that the vanadyl and the niobyl molecules are formed on Al sites and not on P sites. The absolute values for the **g** and **A** tensors of the vanadyl molecule are compatible with the parameters in different minerals (see Tables 4 and 5 in Krambrock et al. 2008). In the montebrasite structure two OH^- or F^- exist that interconnect the Al octahedra along the **c**-axis. The substitution on Al sites is also consistent with the much more compatible ionic radii between V^{4+} (0.58 Å) and Al^{3+} (0.54 Å) compared with P^{5+} (0.34 Å).

The two structurally slightly different distorted Al octahedra, Al1 and Al2, form chains along the **c** direction and are very similar in the montebrasite structure. The difference in the oxygen ligand distances between both octahedra is less than 0.01, 0.05, and 0.2% for the three different types of oxygen neighbors. From the EPR measurements only one magnetically independent site is found. This may be explained by broad linewidths or by preferential occupation of one of the Al octahedron. Figure 8 shows a simplified montebrasite structure indicating the directions of the principal values of the HF and SHF tensors.

The observed hyperfine interactions for both ions are nearly axial and strongest along the **b***-axis, consistent with the observations that both the V and Nb ions substitute for Al and that the principal axes of the HF tensors are pointing to one oxygen neighbor, i.e., the O4 oxygen marked in Figure 8. On the contrary, the superhyperfine interaction is smallest in this direction. Its maximum values are found nearly to the **a**-axis, i.e., 20° off the **a**-axis. From this fact we conclude that the SHF interaction due to two equivalent nuclei with I = ½ (100% abundance) originates from the interaction of the electron spin with 2 equivalent hydrogen ions. These make an angle of about 25° to the **a**-axis, in accordance to the observed angular dependence of the SHF interaction. For equivalent fluorine neighbors the expected SHF

Table 5. Spin Hamiltonian parameters for Fe^{3+}, with same notation as used in Tables 3 and 4

Fe^{3+}	ZZ	YY	XX
g	1.832(6)	2.082(5)	2.131(4)
Θ	113(1)°	90(3)°	23(1)°
Φ	58(1)°	328(1)°	60(6)°
D/h (GHz)	–5.73(1)	–0.64(1)	6.38(1)
Θ	69.3(1)°	67.1(1)°	31.7(1)°
Φ	321.9(1)°	222.6(1)°	89.6(1)°

B_4^0	B_4^1	B_4^2	B_4^3	B_4^4	B_4^{-1}	B_4^{-2}	B_4^{-3}	B_4^{-4}
12(3)	42(3)	–28(3)	–81(6)	36(3)	–50(3)	–25(3)	–73(6)	14(3)

Notes: Fine-structure parameters *D*/*h* and B_4^m are given in GHz and MHz, respectively. Errors are shown in parentheses.

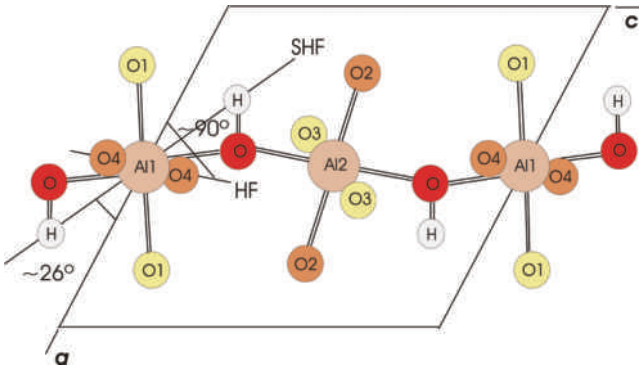

FIGURE 8. Structural arrangement of one chain of the Al octahedra, Al1 and Al2 (pink), in montebrasite projected on the *a*-*c* plane. The two structural slightly different Al1 and Al2 octahedra are interconnected by OH (or F) bonds along the **c**-axis. For simplicity, the PO_4 tetrahedra and the Li ions are omitted (Groat et al. 1990). The principal axes of the *HF* and *SHF* interaction tensors are indicated. Color online.

interaction should be pointing along the **c**-axis, which was not observed. From these facts, we conclude that the vanadyl and also the niobyl molecules are formed on Al1 sites and not on Al2 sites. The reason for this preferential substitution is not clear at the moment. We suggest that the formation of the vanadyl and niobyl molecules in montebrasite is associated to a coupled substitution of $(Al^{3+}\text{-}O^{2-}\text{-}Li^{+})^{2+}$ by $(V^{4+}\text{-}O^{2-})^{2+}$. This suggestion requires the existence of Li vacancies, which are responsible for the charge compensation and even more for the formation of the molecule.

The fluorine-rich montebrasite sample AAZ investigated in this work did not show any EPR spectrum related with Nb or V. In the montebrasite samples AAM, MSN, and MAM, there exist also some F^-, however, it seems that the transition metal ions prefer the incorporation between OH^- ions, which are also necessary to form the complex.

The strongest principal HF interaction of Nb^{4+} is nearly two times that of V^{4+} and minimum interaction of Nb^{4+} is nearly three times that of V^{4+}, which can be explained from the wave functions when comparing the 4d ion with its 3d counterpart. Also the *g* tensor anisotropy for Nb^{4+} is much larger than for V^{4+}. Besides, it is interesting to note that the SHF interaction from two hydrogen ions is also larger for Nb^{4+} than for V^{4+} by a factor of about 2.5. The niobyl EPR spectra were best measured around 80 K, indicating a shorter spin lattice relaxation time when compared with vanadyl. This fact may be related to the electronic structure of the $4d^1$ ion.

The observed EPR spectra of ferric iron (Fe^{3+}) are consistent with the substitutions on Al^{3+} sites, expected from the similar ionic radii in octahedral coordination and equal valence state of both ions. No correlation between the principal axes of the *g* and electronic fine-structure interaction tensors and the local symmetry of the Fe^{3+} site could be established. This behavior can be explained by the low point symmetry C_i for the Al site. Differently to the EPR spectra of vanadyl and niobyl, SHF interaction was not resolved in the spectra. The SHF interaction in the case of Fe^{3+} is hidden in the much broader individual linewidths of about 1.8 mT compared with 0.30 mT of vanadyl and niobyl. It is interesting to note, however, that for low concentrations again only one magnetic inequivalent site was observed.

The electronic fine-structure parameters, $D = -9.57$ GHz and $E = -2.55$ GHz determined for Fe^{3+} in montebrasite are similar to that of Fe^{3+} in euclase and many other minerals (Guedes et al. 2006). As in euclase, Fe^{3+} substitutes for Al^{3+} in a distorted octahedron. Also the determined asymmetry parameter $E/D = 0.27$ is very large and similar to that in euclase. High-spin terms in S^4 are important for Fe^{3+} in montebrasite, however, higher order terms of type BS^3 and BS^5 are practically zero within error, in contrast to the low symmetry Fe^{3+} site in scheelite (Claridge et al. 1997). This fact may be related to the different substitution in montebrasite, where Fe^{3+} substitutes for Al^{3+} compared to the substitution of Fe^{3+} for Ca^{2+} in scheelite for which charge compensation is required. The large zero-field splitting of the *S* state ions, Fe^{3+} with ${}^6S_{5/2}$ ground state, is not well understood yet. In general, covalent binding effects are considered as important and have to be taken into account for the explanation of the large zero-field splitting.

In summary, the detailed EPR analysis of Nb- and V-related ions in montebrasite/amblygonite series shows that both ions form complex defects as vanadyl $(VO)^{2+}$ and niobyl $(NbO)^{2+}$ with spin $S = ½$ on Al1 sites, probably due to a pronounced Jahn-Teller effect induced by nearby Li vacancies. Both complexes show similar symmetry and EPR angular dependence behavior. The present work is a rare case for which $3d^1$ (V^{4+}) ion and $4d^1$ (Nb^{4+}) ion with the same electronic configuration could be compared. As expected the observed HF interaction of Nb ion appears to be larger when compared with that of V ion due to stronger crystal field, stronger spin-orbit coupling and increased amplitude of the wave function near the nucleus. The observed SHF interaction, due to the interaction of two equivalent hydrogen ions, is also larger for Nb compared to V. None of these transition metal ions was observed with F^- neighbors. Montebrasite with much higher fluorine concentrations did not show these transition metal complexes. Fe^{3+} is also incorporated in distorted Al^{3+} ion sites in montebrasite, which show a very large asymmetry ratio E/D of 0.27 for the electronic fine-structure parameters.

ACKNOWLEDGMENTS

The authors are grateful for financial support from the Brazilian agencies FAPEMIG, CNPq, CAPES, and FINEP. Luiz Rodrigues Armoa Garcia (Departamento de Física, UFMG) is acknowledged for performing the electron microprobe analyses.

REFERENCES CITED

Abragam, A. and Bleaney, B. (1986) Electron paramagnetic resonance of transition metal ions. Dover, New York.

Atencio, D., Chukanov, N.V., Coutinho, J.M.V., Menezes Filho, L.A.D., Dubinchuk, V.T., and Möckel, S.T. (2007) Ruifrancoite, a new Fe^{3+}-dominant monoclinic member of the roscherite group from Galiléia, Minas Gerais, Brazil. Canadian Mineralogist, 45, 1263–1273.

Baur, W.H. (1959) Die Kristallstruktur des Edelamblygonits $LiAlPO_4(F,OH)$. Acta Crystallographica, 12, 988–994.

Cerná, I., Cerný, P., and Ferguson, R.B. (1973) The fluorine content and some physical properties of the amblygonite-montebrasite minerals. American Mineralogist, 58, 291–301.

Claridge, R.F., Tennant, W.C., and McGavin, D.G (1997) X-band EPR of Fe^{3+}/$CaWO_4$ at 10K: Evidence for large magnitude high spin Zeeman interactions. Journal of Physics and Chemistry of Solids, 58, 813–820.

Fransolet, A.M. and Tarte, P. (1977) Infrared spectra of analyzed samples of the amblygonite-montebrasite series: A new rapid semi-quantitative determination of fluorine. American Mineralogist, 62, 559–564.

Greiner, D.J. and Bloss, F.D. (1987) Amblygonite-montebrasite optics: Response

to (OH) orientation and rapid estimation of F from 2V. American Mineralogist, 72, 617–624.
Groat, L.A., Raudseep, M., Hawthorne, F.C., Scott Ercit, T., Sheriff, B.L., and Hartman, J.S. (1990) The amblygonite-montebrasite series: Characterization by single-crystal structure refinement, infrared spectroscopy, and multinuclear MAS-NMR spectroscopy. American Mineralogist, 75, 992–1008.
Groat, L.A., Chakoumakos, B.C., Brouwer, D.H., Hoffman, C.A., Morell, H., Fyfe, C.A., and Schultz, A.J. (2003) The amblygonite ($LiAlPO_4F$)-montebrasite ($LiAlPO_4OH$) solid solution: A combined powder and single-crystal neutron diffraction and solid-state ^6Li MAS, CP MAS, and REDOR NMR study. American Mineralogist, 88, 195–210.
Guedes, K.J., Krambrock, K., Pinheiro, M.V.B., and Menezes Filho, L.A.D. (2006) Natural iron-containing blue and colorless euclase studied by electron paramagnetic resonance. Physics and Chemistry of Minerals, 33, 553–557.
Joyce, R.R. and Richards, P.L. (1969) Far-infrared spectra of Al_2O_3 doped with Ti, V, and Cr. Physical Review, 179, 375–380.
Kallio, P. (1978) A new X-ray method for the estimation of fluorine content in montebrasites. American Mineralogist, 63, 1249–1251.
Krambrock, K., Guedes, K.J., and Pinheiro, M.V.B. (2008) Chromium and vanadium impurities in natural green euclase and their relation to the color. Physics and Chemistry of Minerals, 35, 409–415.
Macfarlane, R.M., Wong, J.Y., and Sturge, M.D. (1968) Dynamic Jahn-Teller effect in octahedrally coordinated d^1 impurity systems. Physical Review, 166, 250–258.
McGavin, D.G., Tennant, W.C., and Weil, J.A. (1990) High-spin Zeeman terms in the spin Hamiltonian. Journal of Magnetic Resonance, 87, 92–109.
Rondeau, B., Fritsch, E., Lefevre, P., Guiraud, M., Fransolet, A.-M., and Lulzac, Y. (2006) A Raman investigation of the amblygonite-montebrasite series. Canadian Mineralogist, 44, 1109–1117.
Simonov, W.I. and Belov, N.W. (1958) Die Aufklärung der Struktur des Amblygonits mit Hilfe der Minimumfunktion. Kristallografia, 3, 428–437.
Thiemann, O., Donnerberg, H., Wöhlecke, M., and Schirmer, O.F. (1994) Vibronic structure, energy level and incorporation mechanism of Ti^{3+} in $LiNbO_3$ and $LiTaO_3$. Physical Review B, 49, 5845–5851.
Vassilikou-Dova, A.B. (1993) EPR-determined site distributions of low concentrations of transition-metal ions in minerals: Review and predictions. American Mineralogist, 78, 49–55.

Manuscript received March 8, 2010
Manuscript accepted August 9, 2010
Manuscript handled by M. Darby Dyar